Micromechanics Models for Viscoelastic Plain-Weave Composite Tape Springs

Kawai Kwok*
Technical University of Denmark, 4000 Roskilde, Denmark
and
Sergio Pellegrino[†]
California Institute of Technology, Pasadena, California 91125

The viscoelastic behavior of polymer composites decreases the deployment force and the postdeployment shape accuracy of composite deployable space structures. This paper presents a viscoelastic model for single-ply cylindrical shells (tape springs) that are deployed after being held folded for a given period of time. The model is derived from a representative unit cell of the composite material, based on the microstructure geometry. Key ingredients are the fiber volume density in the composite tows and the constitutive behavior of the fibers (assumed to be linear elastic and transversely isotropic) and of the matrix (assumed to be linear viscoelastic). Finite-element-based homogenizations at two scales are conducted to obtain the Prony series that characterize the orthotropic behavior of the composite tow, using the measured relaxation modulus of the matrix as an input. A further homogenization leads to the lamina relaxation ABD matrix. The accuracy of the proposed model is verified against the experimentally measured time-dependent compliance of single lamina in either pure tension or pure bending. Finite element simulations of single-ply tape springs based on the proposed model are compared to experimental measurements that were also obtained during this study.

Nomenclature

ABD	=	lamina relaxation ABD matrix
a_T	=	temperature shift factor
C	=	tow relaxation modulus tensor
c_1, c_2	=	Williams–Landel–Ferry constants
D	=	uniaxial creep compliance of matrix
d_f	=	fiber diameter
E	=	uniaxial relaxation modulus of matrix
E_L, E_T	=	Young's moduli of fibers
G_{LT}	=	shear modulus of fibers
g	=	tow-to-tow spacing
h	=	maximum tow thickness
L	=	weave length of lamina
l	=	edge length of tow unit cell
M	=	moment resultant
N	=	force resultant
T	=	temperature
T_0	=	reference temperature
t	=	time
t'	=	reduced time
u	=	displacement
v_f	=	fiber volume fraction
x_1, x_2, x_3	=	coordinate system
ϵ	=	strain
θ	=	rotation
κ	=	curvature
ν_{LT}, ν_{TT}	=	Poisson's ratios of fibers
ρ	=	relaxation time
σ	=	stress

*Scientist, Department of Energy Conversion and Storage, Frederiksborgvej 399, Building 779; kwok@dtu.dk.
[†]Joyce and Kent Kresa Professor of Aeronautics and Professor of Civil Engineering, Graduate Aerospace Laboratories, 1200 East California Boulevard, Mail Code 301-46; sergiop@caltech.edu. Fellow AIAA.

I. Introduction

THE release of strain energy stored in thin-shell deployable structures provides a very effective and widely used deployment actuation mechanism, which traditionally has been implemented in the form of open-section, cylindrical thin shells with uniform radius of curvature (tape springs), made of metals such as spring steel or beryllium copper alloys [1–4]. Recently, the higher modulus-to-mass ratio of advanced composite materials and the wider range of shapes that can be made at low cost have motivated research in ultrathin composite deployable structures [5–8], and structures of this kind are increasingly being considered for flight missions. Notable examples of composite deployable structures include the 6.8-m-diam Springback reflector antennas on the Mobile Satellite System [9] and the Mars Advanced Radar for Subsurface and Ionospheric Sounding (MARSIS) antennas on the Mars Express Spacecraft [10,11]. These antennas included two 20 m dipoles and a 7 m monopole, each consisting of a thin-walled closed-section tube with hinges made by cutting slots in the wall of the tube.

Because of the inherent viscoelastic behavior of polymers [12], current knowledge of the strain energy available for deployment after a period of stowage is limited, and the shape precision that can be achieved after deployment has not been quantified. The effects of different temperature environments during stowage and deployment also need to be evaluated. Addressing these problems is important because the MARSIS antenna suffered a significant reduction in deployment moment after a long period of stowage [11].

Recent studies have addressed the viscoelastic behavior of thin-walled deployable structures. For thin shells made of an isotropic and viscoelastic material, the present authors investigated the complete sequence of folding, stowage, and deployment, obtaining continuous measurements of displacement and force [13,14]. Finite element simulations incorporating a linear viscoelastic material model were employed to capture the time-dependent behavior of these structures. For composite structures, Domber et al. [15] measured the shape recovery of a slotted tube under different stowage times. The experimental data were fitted to an exponential series to estimate the viscoelastic time constants. Soykasap [16] studied the deployment dynamics of a folded composite tube and found that increasing the
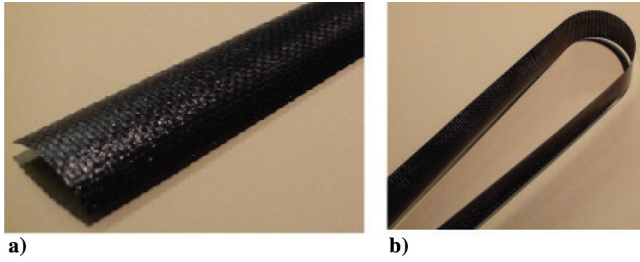
Fig. 1   Composite tape spring: a) deployed, and b) folded.

stowage period results in smaller amplitude of postdeployment vibration but increased duration of this vibration. A recent study of bistable tape springs has shown that viscoelastic relaxation effects can lead to the lower-energy stable configuration becoming unachievable after the shell is held for a sufficiently long period in the higher-energy stable configuration [17].

The effective viscoelastic properties of a fiber-reinforced polymer depend on the constitutive properties of its constituent matrix and fibers as well as the geometry of the fiber tows and the weave geometry. In composite mechanics, homogenization is a well-established tool for determining the effective properties of a composite from the properties and microstructure of the constituent materials. For unidirectional composites, the earliest analytical approaches made use of the elastic–viscoelastic correspondence principle to extend micromechanical models for elastic composites to viscoelastic composites [18–21]. More general results have been obtained from numerical approaches based on either the finite element method [22] or the method of cells [23–25]. For woven composites, semi-analytical models based on simplified weave geometries have been developed [26,27], but comparisons to two-dimensional models have shown only limited accuracy [27]. These predictions have been improved by means of two-dimensional [27] and three-dimensional [28] finite element models of the weave geometry, although only including the in-plane properties of a composite lamina in these models. A computationally efficient multicontinuum approach has been proposed [29].

The purpose of the present paper is to develop a general modeling approach to understand and predict the deployment process of composite thin shells that have been held stowed for an arbitrarily long period of time. The paper is focused on single-layer, plain-weave carbon-fiber-reinforced plastic tape springs and is laid out as follows. Section II provides an outline of linear viscoelasticity theory. In Sec. III, the microstructure of the chosen composite material and the viscoelastic behavior of the matrix are experimentally characterized. Based on these measured properties, in Sec. IV, a two-level multiscale homogenization is developed, which leads to the relaxation *ABD* matrix for the composite shell. Section V presents the implementation details of the homogenization procedure. The resulting viscoelastic model is validated against experimental measurements in Sec. VI. In Sec. VII, the stowage and deployment behavior of composite tape springs, shown in Fig. 1, are then studied in detail. Carefully controlled experiments that characterized the deployment of the tape spring after stowage at different temperatures are presented. A comparison of these experimental results to finite element simulations based on the viscoelastic model developed in the previous sections is also presented. Section VIII concludes the paper.

II.   Review of Linear Viscoelasticity

The constitutive behavior of polymers is dependent on time and temperature and can be modeled with the phenomenological theory of linear viscoelasticity [30–33]. The uniaxial stress–strain relation for isotropic and viscoelastic solids is expressed in terms of the Boltzmann superposition integral,

$$\sigma(t) = \int_0^t E(t-\tau) \frac{d\epsilon(\tau)}{d\tau} \, d\tau \qquad (1)$$

where σ is stress, ϵ is strain, t is time, and E is the uniaxial relaxation modulus expressed as a function of time. An alternative form for this constitutive relation writes the strain as the superposition integral of the creep compliance D and the stress,

$$\epsilon(t) = \int_0^t D(t-\tau) \frac{d\sigma(\tau)}{d\tau} \, d\tau \qquad (2)$$

For implementation in displacement-based finite element solvers, the first formulation is preferred because the stress can be computed directly.

A Prony series can be used to represent the relaxation modulus over a wide range of time scales:

$$E(t) = E_\infty + \sum_{i=1}^n E_i e^{-(t/\rho_i)} \qquad (3)$$

where E_∞ is the long-term modulus, E_i are the Prony coefficients, and ρ_i are the relaxation times. Each exponential term is used to represent the variation of the relaxation modulus over a chosen time period, and the number of terms included in the Prony series depends upon the time range of interest for the problem that is considered.

The temperature dependence of the relaxation modulus is correlated to time through the time–temperature superposition principle, which provides the theoretical foundation to study the long-term behavior of viscoelastic materials using short-term characterization tests. Here, the key assumption is the existence of a shift factor a_T, which is the ratio of the relaxation times at two different temperatures:

$$a_T = \frac{\rho(T)}{\rho(T_0)} \qquad (4)$$

where T is a general temperature, and T_0 is the reference temperature. If the same shift factor applies to all relaxation times, the polymer is described as thermorheologically simple; this is the behavior assumed in the present paper.

A widely used empirical relation for a_T is the Williams–Landel–Ferry equation [34],

$$\log a_T = -\frac{c_1(T - T_0)}{c_2 + (T - T_0)} \qquad (5)$$

in which c_1 and c_2 are material constants that depend on the particular polymer, and the logarithm is of base 10.

The relation between temperature effects and time dependence is captured by introducing the concept of reduced time t', defined as

$$t' = \int_0^t \frac{d\tau}{a_T(T)} \qquad (6)$$

For example, consider the simple case where the temperature is held constant. The reduced time has the expression

$$t' = \frac{t}{a_T} \qquad (7)$$

and hence, substituting Eqs. (5) and (7) into Eq. (3) gives

$$E(t, T) = E(t', T_0) \qquad (8)$$

Equation (8) states that the relaxation modulus at temperature T and time t is the same as that at the reference temperature T_0 and reduced time t'. Hence, it follows that a master curve can be constructed at any arbitrarily chosen reference temperature by shifting to the reference temperature the relaxation moduli at any other temperatures. On a log–log plot of relaxation modulus versus time, this is equivalent to a horizontal shift by $\log a_T(T)$. The resulting master curve is a plot of relaxation modulus that describes

both the time and temperature dependences of the viscoelastic behavior.

In terms of reduced time, the constitutive relation [Eq. (1)] has the expression

$$\sigma(t) = \int_0^t E(t' - \tau') \frac{d\epsilon(\tau)}{d\tau} \, d\tau \tag{9}$$

The relaxation modulus can be characterized either directly by relaxation (constant-strain) tests or by creep (constant-stress) tests followed by a conversion, which can be carried out numerically [35] using the relation

$$\int_0^t E(t - \tau) \frac{dD(\tau)}{d\tau} \, d\tau = 1 \tag{10}$$

The preceding uniaxial constitutive law is extended to three dimensions by writing

$$\sigma_i(t) = \int_0^t C_{ij}(t - \tau) \frac{d\epsilon_j(\tau)}{d\tau} \, d\tau \tag{11}$$

where C is the relaxation modulus tensor, and the stress and strain components are ordered according to the Voigt notation.

A simplified expression for the relaxation modulus tensor is often assumed for isotropic and homogeneous materials, in terms of a single uniaxial relaxation modulus, having assumed a constant Poisson's ratio ν:

$$C(t) = \frac{E(t)}{(1 + \nu)(1 - 2\nu)}$$

$$\times \begin{bmatrix} 1-\nu & \nu & \nu & 0 & 0 & 0 \\ \nu & 1-\nu & \nu & 0 & 0 & 0 \\ \nu & \nu & 1-\nu & 0 & 0 & 0 \\ 0 & 0 & 0 & 1-2\nu & 0 & 0 \\ 0 & 0 & 0 & 0 & 1-2\nu & 0 \\ 0 & 0 & 0 & 0 & 0 & 1-2\nu \end{bmatrix} \tag{12}$$

However, it should be noted that there is no physical basis for this simplified relaxation modulus tensor. The correct relationship has the transverse relaxation coefficients expressed as independent functions [36].

III. Characterization of Plain-Weave T300/PMT-F4

The composite material chosen for the present study was a single-ply plain-weave fabric of T300-1k carbon fibers (manufactured by Toray Industries) impregnated with PMT-F4 (manufactured by Patz Materials and Technologies) epoxy resin. The properties of these materials are provided in Table 1 ([37]).‡ Composite specimens were fabricated by curing the resin-impregnated fabric under vacuum for 2 h at a temperature of 120°C and a consolidation pressure of 400 kPa.

The viscoelastic response of this material depends on the tow and weave geometries as well as the constitutive behavior of the matrix and the fibers. The experimental determination of these properties, which are a necessary input for the homogenization procedure, is presented next.

A. Geometry of Tows and Fabric Weave

The geometries of the carbon-fiber tows and the fabric weave were characterized using optical microscopy. The cured composite was sectioned, embedded in an epoxy resin mold, and then ground and polished. Images of these sections were then taken using a Nikon Eclipse LV100 microscope with a Nikon DS-Fi1 digital camera.

‡Private communication from Patz Materials and Technologies.

Table 1 Properties of fibers and fabric [37] and PMT-F4 matrix (see footnote §)

Parameter	Value
Diameter of T300 fiber (d_f)	7 μm
Density of T300 fiber (ρ_f)	1760 kg/m³
Areal density of T300-1k fabric (w_f)	0.098 kg/m²
Density of PMT-F4 matrix (ρ_m)	1220 kg/m³

The following geometric properties were measured from micrographs of three 10-mm-long sections. For example, Fig. 2 shows a representative part of a tow cross section. The fibers were distinguished from the matrix by setting an intensity threshold based on visual inspection of the intensity histogram. The fiber volume fraction of a tow was determined by determining the area occupied by fibers within a sampling area of $50 \times 50 \ \mu$m. The analysis was carried out on five tow cross sections, and the averaged fiber volume fraction was found to be $v_f = 0.64$. Image analysis of the partitioned image also verified the fiber diameter to be $d_f = 7.0 \ \mu$m.

Figure 3 shows a longitudinal section of a fill tow and cross sections of two warp tows. The tow width w was determined by visual inspection of the edges of each tow cross section. The midpoint of each tow was found from the defined tow width, and the distance between midpoints of neighboring tows was defined to be half the weave length, $L/2$. The tow spacing g is the distance between edges of neighboring tows. Five measurements were taken for each parameter. The overall fiber volume fraction was determined from

$$v_f = \frac{w_f \rho_m}{w_f \rho_m + (w_c - w_f)\rho_f} \tag{13}$$

where w_c is the areal weight of the composite, found to be $w_c = 0.161$ kg/m² by averaging weight measurements of five 100×100 mm specimens. The overall fiber volume fraction was calculated to be $v_f = 0.52$. The other properties were: weave length $L = 3.5$ mm, maximum tow thickness $h = 0.063$ mm, tow width $w = 1.05$ mm, and tow spacing $g = 0.7$ mm.

B. Viscoelastic Model of Matrix

The epoxy matrix was treated as an isotropic, viscoelastic material. Its behavior was characterized according to the linear viscoelasticity theory reviewed in Sec. II.

The uniaxial master curve was obtained from uniaxial creep tests on samples that were laser cut from 2.9-mm-thick sheets made by curing neat PMT-F4 resin at 120°C for 2 h, with a temperature control precision of ±2°C. The samples were 96.5 mm long by 12.1 mm wide rectangles.

Tensile creep tests were performed using an Instron 5500 materials testing machine fitted with a 1 kN load cell. An Instron Heatwave Model 3119-506 environmental chamber with a built-in thermocouple to control the temperature with a precision of ±1°C was used for these tests. A type-T thermocouple made of copper/constantan was attached to the surface of a dummy sample close to the test sample. The stability of the temperature conditioning inside the environmental chamber was measured by prescribing a temperature impulse and recording the subsequent temperature variation over time, both with the built-in
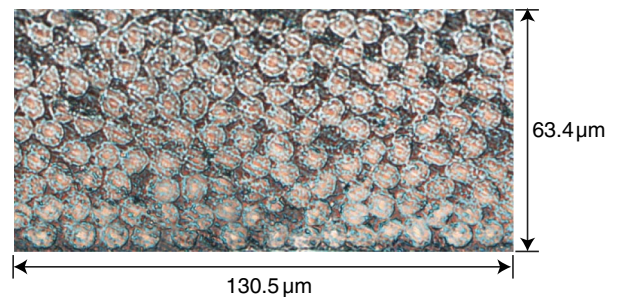

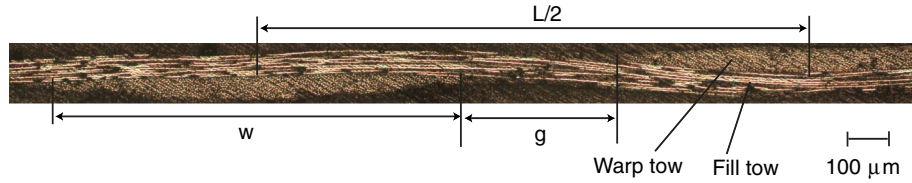**Fig. 2 Representative cross section of a tow.**

63.4 μm

130.5 μm

Fig. 3   Longitudinal section of a fill tow, also showing cross sections of two warp tows.

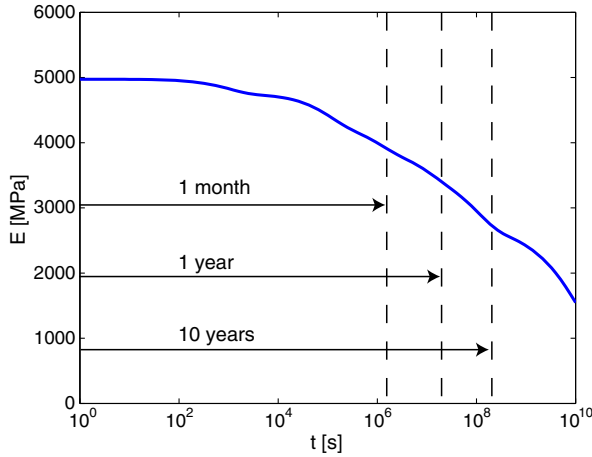**Fig. 4   Uniaxial relaxation modulus master curve of PMT-F4 epoxy at $T_0 = 40°C$.**

thermocouple and the dummy thermocouple. It was found that the temperature readings from the two thermocouples became identical 30 min after the impulse, indicating that thermal equilibrium is established within such time frame. Hence, this thermal conditioning delay was allowed before each test.

Creep tests were conducted at temperatures ranging from 20 to 90° C, at 10°C intervals. Before each test, the sample was clamped by grips, and the temperature of the chamber was brought to the specified value while manually adjusting the extension of the sample to keep the reading from the load cell close to zero. Once the test temperature had been reached, a fine adjustment of the position of the loading beam was carried out, to bring the load cell reading to a zero mean, and finally the sample was left to relax for 30 min. In each test, a load of 106.7 N (corresponding to a stress of 3.0 MPa) was applied in 225 s, and this load was held constant for 3 h. The time-varying longitudinal strain was measured using a laser extensometer (Electronic Instrument Research Ltd LE-05) recording at a rate of 5 Hz.

The measured longitudinal strain and the applied stress were first used to obtain the creep compliance using Eq. (2). Assuming the stress to be applied instantaneously, it can be represented mathematically with a Heaviside step function. Equation (2) becomes

$$\epsilon(t) = D(t)\sigma_0 \qquad (14)$$

where σ_0 is the applied stress magnitude. Because the actual loading profile was a ramp, the measured strain response would deviate from that in the ideal case of instantaneous loading. The difference, however, becomes negligible after a period of 10 times the ramp time has elapsed [38]. For this reason, the strain data measured during the first 2500 s were discarded.

Once a plot of the creep compliance at each temperature had been obtained, it was shifted to the reference temperature $T_0 = 40°C$ to obtain the master curve. The shift factors were determined such that the shifted creep compliances form a single smooth curve. A Prony series was fitted to the creep compliance master curve and then numerically converted to a series representation of the relaxation modulus using Eq. (10).

Figure 4 shows the Prony series representation of the relaxation modulus master curve of PMT-F4 at the reference temperature of

$T_0 = 40°C$. Table A1 lists the corresponding Prony series parameters. The material constants c_1 and c_2 were found by fitting the temperature shift data to Eq. (5). The values obtained are

$$c_1 = 28.3816 \quad \text{and} \quad c_2 = 93.291$$

As already discussed in Sec. II, a constant Poisson's ratio was assumed. A typical value of 0.33 was chosen.

C.   Elastic Model of Fibers

The carbon fibers (T300, manufactured by Toray) were assumed to be linear elastic and transversely isotropic [39]. The elastic constants provided by the manufacturer are listed in Table 2.

IV.   Micromechanics Model of Plain-Weave Composite

A viscoelastic model for a single-ply, plain-weave composite lamina was derived on the basis of Kirchhoff plate theory (midplane normals remaining normal to the deformed midplane). The model parameters are the Prony coefficients of the relaxation *ABD* matrix, relating midplane strains and curvatures to midplane force and moment resultants for a representative unit volume of the composite, defined according to the microstructural geometry and material properties presented in Sec. III. The model was obtained from a two-step homogenization procedure, as described next.

A.   Viscoelastic Model of Tows

Unit cell homogenization of unidirectional fiber composites was first used in [22] to determine their effective viscoelastic properties. This reference obtained the plain-strain relaxation modulus from a two-dimensional unit cell.

The tow unit cell was defined as a three-dimensional, transversely isotropic solid consisting of a single fiber surrounded by matrix, thus implicitly assuming a square array fiber arrangement. Hexagonal array and random array fiber arrangements were also implemented, but the difference between these configurations was found to be insignificant at the volume fraction of interest. The model consisted of a cube with edge length of $\ell = 7.7\ \mu$m, as shown in Fig. 5. The fiber diameter and volume fraction of the unit cell were given the vales provided in Sec. III.A. The matrix was defined as linear–viscoelastic and isotropic, as in Sec. III.B. The fiber was defined as linear–elastic and transversely isotropic, as in Sec. III.C.

Under a uniform applied stress or strain, the resulting strain and stress fields within the unit cell are nonuniform because the properties of the constituents are different. The stress and strain in the homogenized tow were defined as the volume averages of the heterogeneous stress and strain fields within the unit cell, and the effective (homogenized) properties of the tow were defined by the constitutive relations between such volume-averaged stress and strain.

Table 2   Elastic properties of T300 carbon fibers

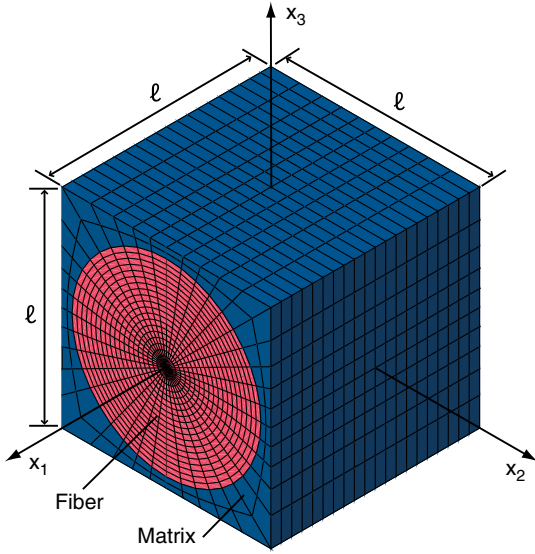| Parameter	Value
Longitudinal modulus E_L	233,000 MPa
Transverse modulus E_T	23,100 MPa
Shear modulus G_{LT}	8963 MPa
Longitudinal Poisson's ratio ν_{LT}	0.2
Transverse Poisson's ratio ν_{TT}	0.4

Fig. 5 Finite element mesh of tow unit cell.

The volume averages of the strain and stress fields are given by

$$\bar{\epsilon}_i = \frac{1}{V} \int_V \epsilon_i \, dV \qquad (15)$$

$$\bar{\sigma}_i = \frac{1}{V} \int_V \sigma_i \, dV \qquad (16)$$

where V is the volume of the unit cell, and the overbar denotes the volume average taken over V.

The effective constitutive equation for the viscoelastic tow is given by

$$\bar{\sigma}_i(t) = \int_0^t C_{ij}(t - \tau) \frac{d\bar{\epsilon}_j(\tau)}{d\tau} \, d\tau \qquad (17)$$

where C is the effective relaxation modulus tensor of the tow, and the strain components are defined with respect to the coordinate directions shown in Fig. 5 and are ordered as follows:

$$\epsilon_1 = \epsilon_{11},$$

$$\epsilon_2 = \epsilon_{22},$$

$$\epsilon_3 = \epsilon_{33},$$

$$\epsilon_4 = \epsilon_{23},$$

$$\epsilon_5 = \epsilon_{13},$$

$$\epsilon_6 = \epsilon_{12} \qquad (18)$$

The unit cell is symmetric about the plane of isotropy $x_2 - x_3$, and hence, the effective relaxation modulus tensor of the tow has the form

$$C = \begin{bmatrix} C_{11} & C_{12} & C_{13} & 0 & 0 & 0 \\ C_{12} & C_{22} & C_{23} & 0 & 0 & 0 \\ C_{13} & C_{23} & C_{22} & 0 & 0 & 0 \\ 0 & 0 & 0 & C_{44} & 0 & 0 \\ 0 & 0 & 0 & 0 & C_{55} & 0 \\ 0 & 0 & 0 & 0 & 0 & C_{55} \end{bmatrix} \qquad (19)$$

where the coefficient C_{44} is related to C_{22} and C_{23} by [39]

$$C_{44} = \frac{C_{22} - C_{23}}{2} \qquad (20)$$

The objective of the homogenization is therefore to determine the five independent coefficients C_{11}, C_{22}, C_{12}, C_{23}, and C_{55}. Each

coefficient is described by a Prony series having the same relaxation times as the epoxy matrix (see Table A1) but different Prony coefficients:

$$C_{ij} = C_{ij,\infty} + \sum_{k=1}^n C_{ij,k} e^{-(t/\rho_k)} \qquad (21)$$

In other words, the parameters to be computed are the Prony coefficients for each of five coefficients in the effective relaxation modulus tensor.

For example, to obtain $C_{55}(t)$, a step function was assigned to $\bar{\epsilon}_5(t)$, with all other strain components set to zero. The computed response $\sigma_5(t)$ was averaged over the unit cell volume, using Eq. (17), and the corresponding volume average $\bar{\sigma}_5(t)$ was obtained. By choosing $\bar{\epsilon}_5(t)$ as a step function, $\bar{\sigma}_5(t)$ represents the stress relaxation, which can be fitted to Eq. (21) to obtain the Prony coefficients for $C_{55}(t)$. The Prony coefficients of the other components were determined in a similar manner. More details are provided in Sec. V.A.

B. Viscoelastic Model of Plain-Weave Laminas

The lamina was modeled as a viscoelastic Kirchhoff plate, whose relaxation *ABD* matrix was derived from the homogenization described in this section.

The lamina unit cell includes four tows, whose properties are defined according to Sec. IV.A, and regions of neat resin in between, as shown in Fig. 6. The geometry of the unit cell, defined to closely represent the weave geometry described in Sec. III.A, consists of four identical solids with four-fold symmetry about the central, vertical axis. Each solid consists of a tow region and a resin region, with the boundary surfaces defined by sinusoidal functions. This definition, which uses only the geometric parameters in Sec. III.A, leads to no gaps or no overlaps. For example, the boundaries of the solid in Fig. 6b are given by

$$x_3 = \pm \frac{h}{2} \sin\left(\frac{2\pi x_1}{L}\right) + \frac{h}{2} \sin\left(\frac{2\pi x_2}{L}\right) \qquad (22)$$

The matrix was defined to have the viscoelastic, isotropic behavior defined in Sec. III.B. The tow was defined as viscoelastic and transversely isotropic, with the properties obtained from the homogenization described in Sec. IV.A.

The constitutive equations for a viscoelastic Kirchhoff plate can be obtained by using Eq. (1) in the derivation of the *ABD* matrix in classical lamination theory [39]. The outcome is

$$N_i(t) = \int_0^t \left(A_{ij}(t - \tau) \frac{d\epsilon_j(\tau)}{d\tau} + B_{ij}(t - \tau) \frac{d\kappa_j(\tau)}{d\tau} \right) d\tau \qquad (23)$$

$$M_i(t) = \int_0^t \left(B_{ij}(t - \tau) \frac{d\epsilon_j(\tau)}{d\tau} + D_{ij}(t - \tau) \frac{d\kappa_j(\tau)}{d\tau} \right) d\tau \qquad (24)$$

where N_i and M_i are the force and moment resultant components, and ϵ_j and κ_j are the midplane strains and out-of-plane curvatures of the midplane, defined by

$$\epsilon_1 = \frac{\partial u_1}{\partial x_1} \qquad (25)$$

$$\epsilon_2 = \frac{\partial u_2}{\partial x_2} \qquad (26)$$

$$\epsilon_3 = \frac{\partial u_1}{\partial x_2} + \frac{\partial x_2}{\partial x_1} \qquad (27)$$
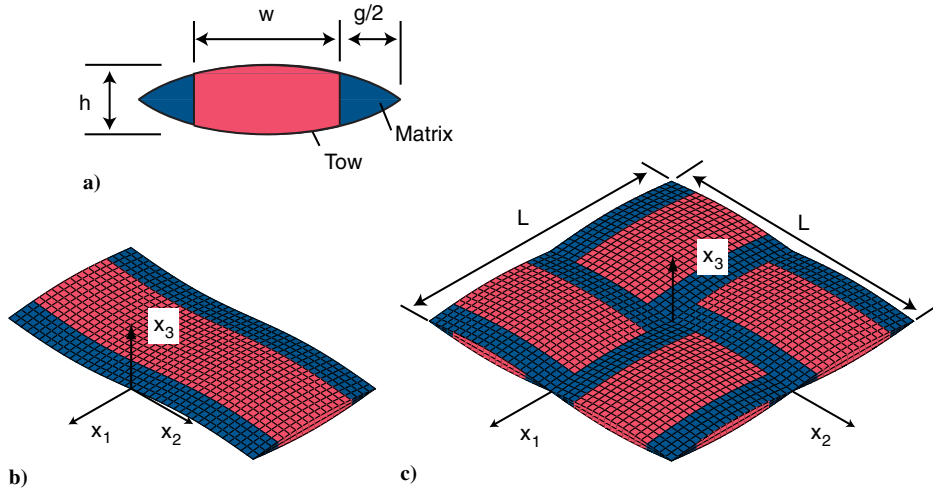
Fig. 6   Finite element model for lamina unit cell: a) section of tow and edge matrix, b) single tow, and c) complete unit cell.

$$\kappa_1 = -\frac{\partial^2 u_3}{\partial x_1^2} \tag{28}$$

$$\kappa_2 = -\frac{\partial^2 u_3}{\partial x_2^2} \tag{29}$$

$$\kappa_3 = -2\frac{\partial^2 u_3}{\partial x_1 \partial x_2} \tag{30}$$

The time-dependent submatrices, A, B, and D represent the in-plane, stretching–bending coupling, and bending relaxation moduli. The directional properties of a plain-weave lamina resemble those of symmetric cross-ply laminas. In particular, $A_{11} = A_{22}$ and $D_{11} = D_{22}$, because the fill and warp tows have identical properties; $A_{13} = A_{23} = 0$, indicating that stretching and shearing are decoupled; and $D_{13} = D_{23} = 0$ because bending and twisting are also decoupled. The entire submatrix B is zero because there is no coupling between in-plane and out-of-plane behavior. Hence, the ABD matrix has the following structure:

$$
ABD = \begin{bmatrix}
A_{11} & A_{12} & A_{13} & B_{11} & B_{12} & B_{13} \\
A_{12} & A_{22} & A_{23} & B_{12} & B_{22} & B_{23} \\
A_{13} & A_{23} & A_{33} & B_{13} & B_{23} & B_{33} \\
B_{11} & B_{12} & B_{13} & D_{11} & D_{12} & D_{13} \\
B_{12} & B_{22} & B_{23} & D_{12} & D_{22} & D_{23} \\
B_{13} & B_{23} & B_{33} & D_{13} & D_{23} & D_{33}
\end{bmatrix}
$$

$$
= \begin{bmatrix}
A_{11} & A_{12} & 0 & 0 & 0 & 0 \\
A_{12} & A_{11} & 0 & 0 & 0 & 0 \\
0 & 0 & A_{33} & 0 & 0 & 0 \\
0 & 0 & 0 & D_{11} & D_{12} & 0 \\
0 & 0 & 0 & D_{12} & D_{11} & 0 \\
0 & 0 & 0 & 0 & 0 & D_{33}
\end{bmatrix} \tag{31}
$$

The coefficients of this matrix were determined numerically, following a process analogous to that followed in Sec. IV.A. Unit step variations of the midplane strains and curvatures were imposed on the lamina unit cell, and the corresponding, time-dependent force and moment resultants were calculated from a series of finite element analyses. The coefficients of the ABD matrix were then obtained by fitting these computed responses to Prony series having the same relaxation times as the matrix, but different coefficients:

$$A_{ij} = A_{ij,\infty} + \sum_{k=1}^{n} A_{ij,k} e^{-(t/\rho_k)} \tag{32}$$

$$D_{ij} = D_{ij,\infty} + \sum_{k=1}^{n} D_{ij,k} e^{-(t/\rho_k)} \tag{33}$$

V.   Numerical Implementation

This section describes the implementation of the two-scale homogenization presented in Sec. IV using the commercial finite element software ABAQUS/Standard [40].

A.   Tow Relaxation Modulus Tensor

The finite element mesh for the tow unit cell (Fig. 5) consisted of 16,800 eight-node brick elements and 800 six-node triangular prism elements (respectively elements C3D8 and C3D6 in ABAQUS). The elements representing the matrix were defined as viscoelastic, with the Prony series presented in Table A1 and a time-independent Poisson's ratio of 0.33. The elements representing the fibers were defined as linear–elastic, with the properties given in Table 2.

Periodic displacement boundary conditions were enforced between each pair of nodes on opposite boundary faces of the unit cell, through the following constraint equations:

$$u_1\left(\frac{\ell}{2}, x_2, x_3\right) - u_1\left(-\frac{\ell}{2}, x_2, x_3\right) = \bar{\epsilon}_1 \ell \tag{34}$$

$$u_2\left(\frac{\ell}{2}, x_2, x_3\right) - u_2\left(-\frac{\ell}{2}, x_2, x_3\right) = \bar{\epsilon}_6 \ell \tag{35}$$

$$u_3\left(\frac{\ell}{2}, x_2, x_3\right) - u_3\left(-\frac{\ell}{2}, x_2, x_3\right) = \bar{\epsilon}_5 \ell \tag{36}$$

$$u_1\left(x_1, \frac{\ell}{2}, x_3\right) - u_1\left(x_1, -\frac{\ell}{2}, x_3\right) = \bar{\epsilon}_6 \ell \tag{37}$$

$$u_2\left(x_1, \frac{\ell}{2}, x_3\right) - u_2\left(x_1, -\frac{\ell}{2}, x_3\right) = \bar{\epsilon}_2 \ell \tag{38}$$

$$u_3\left(x_1, \frac{\ell}{2}, x_3\right) - u_3\left(x_1, -\frac{\ell}{2}, x_3\right) = \bar{\epsilon}_4 \ell \tag{39}$$

$$u_1\left(x_1, x_2, \frac{\ell}{2}\right) - u_1\left(x_1, x_2, -\frac{\ell}{2}\right) = \bar{\epsilon}_5 \ell \tag{40}$$
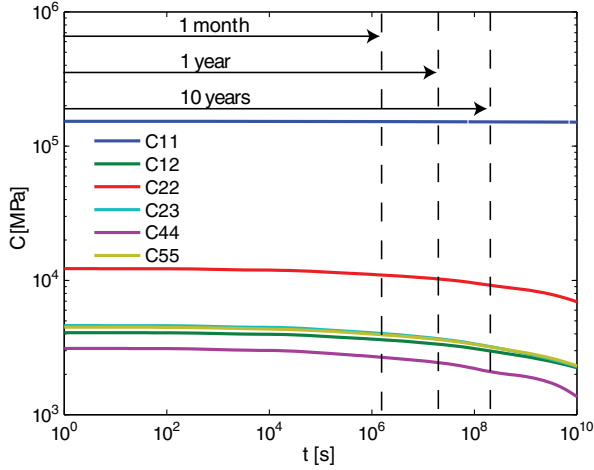
Fig. 7   Tow relaxation moduli.

$$u_2\left(x_1, x_2, \frac{\ell}{2}\right) - u_2\left(x_1, x_2, -\frac{\ell}{2}\right) = \bar{e}_4\ell \qquad (41)$$

$$u_3\left(x_1, x_2, \frac{\ell}{2}\right) - u_3\left(x_1, x_2, -\frac{\ell}{2}\right) = \bar{e}_3\ell \qquad (42)$$

where u_1, u_2, and u_3 denote displacement components in the x_1, x_2, and x_3 directions, respectively. In the finite element representation of these equations, each of the six volume-averaged strain components was associated with an arbitrary displacement degree of freedom of a dummy node. The desired value of the applied strain was prescribed by specifying the displacement of the respective dummy node.

Three separate analyses were required to determine the five independent components in the relaxation modulus tensor C because each analysis provides a full column of coefficients. Each analysis consisted of two steps, defined with the option quasi-static *VISCO in ABAQUS. In the first step, which simulates the application of an instantaneous strain, a unit amplitude of one of the three strain variables ($\bar{e}_1$, $\bar{e}_2$, and $\bar{e}_5$) was applied to the unit cell over a very short time period ($\times 10^{-10}$ s). This short time duration was chosen such that the tow would behave elastically. All other strain variables were set to zero. During the second step, which lasted 10^{10} s, the applied strains were held constant.

After each analysis, the time-dependent, corresponding volume-averaged stress components were obtained by dividing the reaction forces at the dummy nodes, computed by ABAQUS, by the area of the unit cell boundary face. To obtain the values of the Prony coefficients, the computed time history was fitted to Eq. (21) using the Levenberg–Marquardt optimization algorithm in Matlab.

The independent coefficients of C, obtained in this way, are plotted in Fig. 7. Note that C_{11} has a much weaker time dependence than the other moduli because the behavior in the fiber direction is dominated by the time-independent behavior of the fibers. The Prony coefficients are listed in Table A2.

B.   Lamina Relaxation Matrix

Each of the four tows forming the lamina unit cell (Fig. 6) was meshed with 960 eight-node brick elements, and the matrix regions along the edges of the tows were meshed with 1920 eight-node brick and 640 six-node triangular prism elements. The tow elements were defined as viscoelastic, with the relaxation modulus tensor C obtained in Sec. V.A, through a user-defined material subroutine. The elements representing the matrix were given the viscoelastic properties of PMT-F4, in Table A1.

To impose the constraint that the normals to the midplane of the lamina remain orthogonal to the deformed midplane (Kirchhoff plate model), the nodes lying on the boundary faces of the unit cell were tied to the midplane nodes through rigid connectors. The displacements and rotations of each midplane node on one face were

paired to those of a corresponding node on the opposite face by constraint equations that impose periodic boundary conditions in terms of midplane strains and out-of-plane curvatures. The constraint equations for this problem were given by Kueh and Pellegrino [41]:

$$u_1\left(\frac{L}{2}, x_2\right) - u_1\left(-\frac{L}{2}, x_2\right) = \epsilon_1 L \qquad (43)$$

$$u_2\left(\frac{L}{2}, x_2\right) - u_2\left(-\frac{L}{2}, x_2\right) = \frac{1}{2}\epsilon_3 L \qquad (44)$$

$$u_3\left(\frac{L}{2}, x_2\right) - u_3\left(-\frac{L}{2}, x_2\right) = -\frac{1}{2}\kappa_3 x_2 L \qquad (45)$$

$$\theta_1\left(\frac{L}{2}, x_2\right) - \theta_1\left(-\frac{L}{2}, x_2\right) = -\frac{1}{2}\kappa_3 L \qquad (46)$$

$$\theta_2\left(\frac{L}{2}, x_2\right) - \theta_2\left(-\frac{L}{2}, x_2\right) = \kappa_1 L \qquad (47)$$

$$\theta_3\left(\frac{L}{2}, x_2\right) - \theta_3\left(-\frac{L}{2}, x_2\right) = 0 \qquad (48)$$

$$u_1\left(x_1, \frac{L}{2}\right) - u_1\left(x_1, -\frac{L}{2}\right) = \frac{1}{2}\epsilon_3 L \qquad (49)$$

$$u_2\left(x_1, \frac{L}{2}\right) - u_2\left(x_1, -\frac{L}{2}\right) = \epsilon_2 L \qquad (50)$$

$$u_3\left(x_1, \frac{L}{2}\right) - u_3\left(x_1, -\frac{L}{2}\right) = -\frac{1}{2}\kappa_3 x_1 L \qquad (51)$$

$$\theta_1\left(x_1, \frac{L}{2}\right) - \theta_1\left(x_1, -\frac{L}{2}\right) = -\kappa_2 L \qquad (52)$$

$$\theta_2\left(x_1, \frac{L}{2}\right) - \theta_2\left(x_1, -\frac{L}{2}\right) = \frac{1}{2}\kappa_3 L \qquad (53)$$

$$\theta_3\left(x_1, \frac{L}{2}\right) - \theta_3\left(x_1, -\frac{L}{2}\right) = 0 \qquad (54)$$

where θ_1, θ_2, and θ_3 are rotations about the x_1, x_2, and x_3 axes, respectively. In the finite element model, each of the six deformation components (ϵ_1, ϵ_2, ϵ_3, κ_1, κ_2, κ_3) is associated with an arbitrary displacement degree of freedom of a dummy node. The desired applied deformation was prescribed by specifying a particular displacement of the respective dummy node.

The time-dependent coefficients of the relaxation ABD matrix for the lamina unit cell were determined by carrying out six separate analyses. In each analysis, a unit step amplitude of one of the six deformation variables was applied to the unit cell, over a short time period (1×10^{-10} s), and was then held constant. Meanwhile, all other deformation variables were held equal to zero. The time variations of the force and moment resultants were obtained from the reactions at the dummy nodes and fitted to Eqs. (32) and (33), again using the Levenberg–Marquardt algorithm in Matlab, to obtain the Prony coefficients for the ABD matrix of the lamina, defined in Eq. (31).
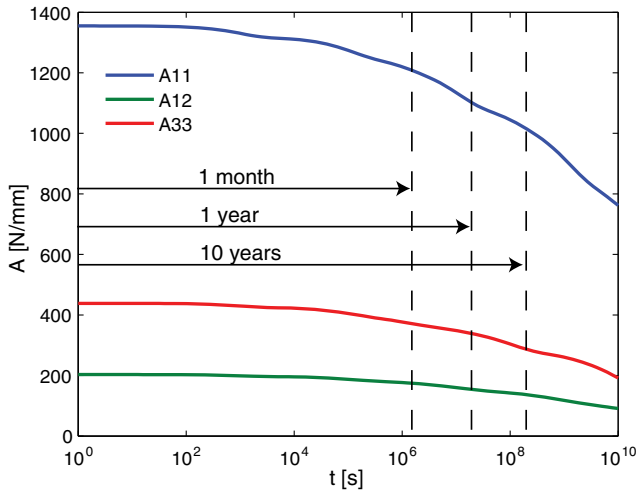
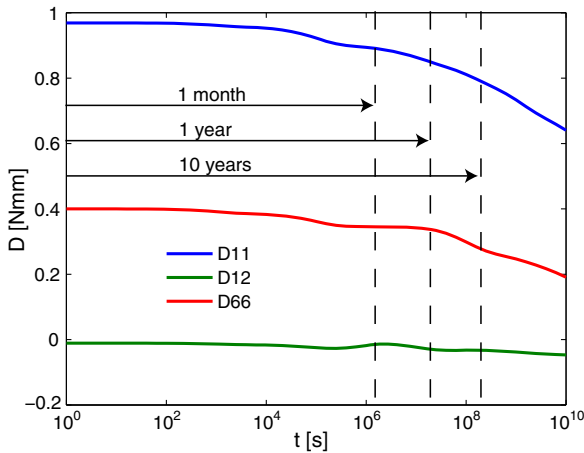Fig. 8   In-plane relaxation coefficients of single-ply lamina.

Fig. 9   Bending relaxation coefficients of single-ply lamina.

Fig. 10   Longitudinal stretching compliance of ±45° plain-weave lamina at 40°C.
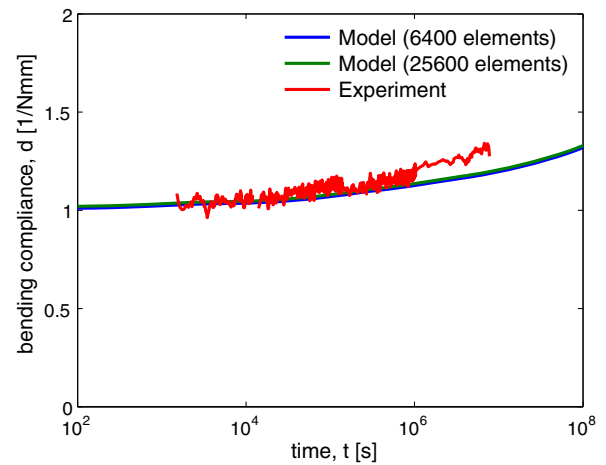
Fig. 11   Longitudinal bending compliance of ±45° plain-weave lamina at 40°C.

The six nonzero coefficients (A_{11}, A_{12}, A_{33}, D_{11}, D_{12}, and D_{33}) completely characterize the effective viscoelastic behavior of the lamina; they are plotted in Figs. 8 and 9. The numerical values of the Prony coefficients are listed in Tables A3 and A4.

VI.   Model Verification

The viscoelastic model for the lamina was verified against uniaxial tension and four-point bending creep experiments conducted on single-ply ±45 laminas. The length of all test samples was 100 mm, and the width was 20 mm for the tension samples and 50 mm for the bending samples. In the tension tests, a force of 30 N was applied over 30 s and held constant for 10^4 s. The creep strain of the samples was measured continuously over time. For the bending tests, the span between the inner loading pins was 10 mm, and a force of 0.8 N was applied over a period of 10 s. The vertical deflection of the midpoint of the sample was measured. Each type of test was repeated twice, at three temperatures (50, 60, and 70°C).

The longitudinal stretching compliance was obtained from the tension test results, by dividing the measured strain by the applied stress. The bending compliance d was calculated from the applied moment and midpoint deflection, using the viscoelastic Euler–Bernoulli beam relationship,

$$\delta(t) = \frac{Ps^3}{4I} d(t) \qquad (55)$$

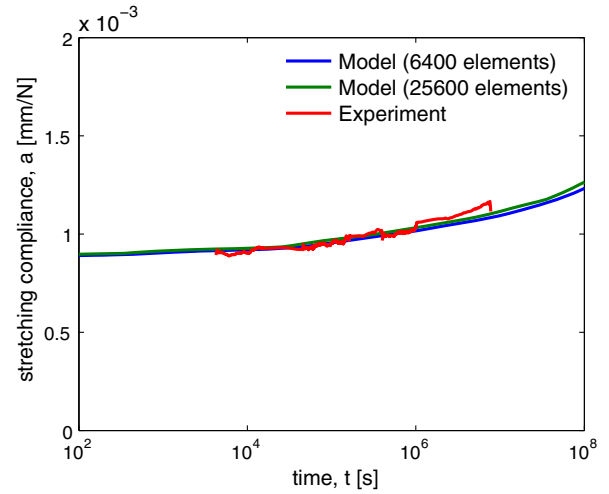where δ is the midpoint deflection, P is the applied load in the four-point bending test, s is the half-distance between the inner loading pins (with $4s$ being the total distance between the outer loading pins), and I is the second moment of area of the sample.

The results from the two tests at each temperature were averaged, and the compliances at different temperatures were shifted to the reference temperature, using the time shifts derived in Sec. III.B.

Model predictions for the measured compliances were obtained by carrying out tension and bending creep analyses on the lamina unit cell. The applied force and moment used in the tests were first converted to force and moment resultants and then transformed to the coordinate frame of the lamina unit cell. The resulting midplane strains and curvatures computed from the unit cell model were transformed back to the longitudinal direction of the sample. The results are plotted in Figs. 10 and 11.

Generally, good agreement was obtained between model predictions and experimental measurements, but the experimental bending compliances were noisier than the extensional ones, due to vibration caused by air circulation inside the environmental chamber. Note that no filtering or smoothing has been applied to the experimental results.

VII.   Deployment of Tape Springs

A.   Experiments

The deployment behavior of tape springs that had been held folded for a period of time was studied experimentally. The tests were carried out on 596-mm-long tape springs with transverse radius of 19 mm, thickness of 0.125 mm, and areal density of 160.7 g/m², made from ±45 plain-weave fabric with 1k tows of T300 carbon fibers

impregnated with PMT-F4 epoxy resin. The tape springs had been fabricated by laying the resin-impregnated fabric on a cylindrical steel mandrel, wrapping the assembly in release films, and curing under vacuum for 2 h at 120°C and 400 kPa. A fiber orientation at 45 deg to the axis of the tape spring was chosen to display relatively large viscoelastic effects in both the deployment behavior (dominated by the longitudinal in-plane stiffness of the tape spring) and the end-of-deployment snap into the fully deployed configuration (dominated by the transverse bending stiffness of the tape spring).

The test design took into account the temperature dependence of the relaxation time. The epoxy matrix has a glass transition temperature T_g well above room temperature; therefore, at room temperature, it is only weakly viscoelastic and hence would need to be held folded for a long time to observe noticeable viscoelastic effects. Because relaxation/creep behavior accelerates at temperatures closer to T_g, the tape spring was held folded at a temperature higher than room temperature.

In each test, the tape spring was first held folded for a given length of time at a specified temperature and then deployed at different temperatures; the shape change during deployment was measured. Experiments were performed inside a thermal chamber that stabilizes the temperature within 0.1°C over the test period. The tape spring was clamped at the bottom end and positioned vertically on a granite table. Thermocouples were placed at three different locations in the vicinity of the tape spring to monitor the temperature uniformity, which could be controlled within ±0.5°C.

In a previous study [14], it was discovered that the behavior of viscoelastic tape springs is characterized by a relatively fast deployment followed by a short-term oscillatory phase, and followed by a long-term recovery phase. During the short-term deployment and oscillatory phases, there are visible rotations at the fold location, but during the final recovery phase, the overall shape changes are relatively small. To capture both of these behaviors, two displacement measurement schemes were employed to probe the behavior under such different length and time scales, as described next. A high-resolution Sony Handycam HDR-XR500V digital camcorder with a rate of 30 frames per second was used to obtain side images of the tape spring, from which the deployment angle could be measured. The three-dimensional digital image-correlation system Vic-3D was used to obtain full-field displacement/strain measurements of the fold region in the tape spring, during the recovery phase. The Vic-3D system, developed by Correlated Solutions, consists of two Point Grey Research charge-coupled device cameras with a resolution of 2448 × 2048 and a pixel size of 3.45 × 3.45 μm. The cameras were positioned such as to capture images of the inner (concave) surface of the tape spring throughout the test. The experimental configuration is shown in Fig. 12.

The test procedure was as follows. The chamber was first heated and stabilized at the stowage temperature. The chamber was then opened, and the tape spring was manually folded to an angle of 87 deg, as shown in the figure. To minimize the disturbance of the thermal environment, the chamber was kept open for only a short time. The tape spring was held in this folded configuration for a
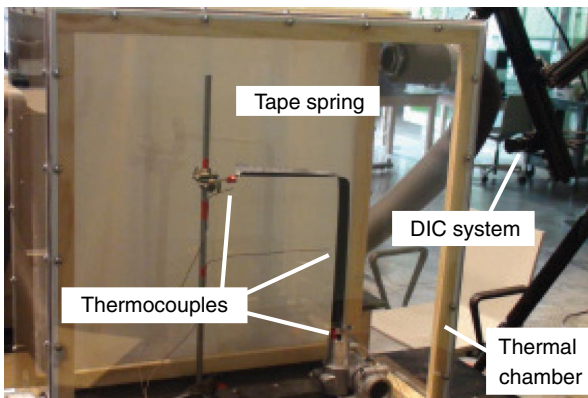
Table 3   Thermal conditions of tests on tape springs

Test	Stowage temperature, °C	Deployment temperature, °C
1	23	23
2	60	60
3	60	23

period of 8 h, by attaching a string between the granite table and the free end of the tape spring. After the stowage period, the temperature inside the chamber was changed to the deployment temperature, and deployment of the tape spring was initiated by passing an electrical current through a Nichrome wire attached to the string. Images of the tape spring were recorded from the start of deployment, for a duration of 8 h. The stowage and deployment temperatures in each test are summarized in Table 3. Note that each test was repeated under nominally identical conditions; the results presented here are averages of two nominally identical experiments.

B. Simulations

The deployment behavior of the tape spring was simulated with the finite element software ABAQUS/Standard. The finite element model of the tape spring consisted of 2268 quadrilateral shell elements with a maximum dimension of 3.85 mm, as shown in Fig. 13. The viscoelastic behavior of the shell elements was defined by assigning the *ABD* matrix obtained in Sec. V.B via a user-defined shell section subroutine.

The boundary conditions were applied as follows. The bottom end section CC' was held fixed throughout the analysis. To reach the folded configuration, the cross section at the fold region was first flattened by applying equal and opposite rotations on the two edge nodes B and B'. At the same time, a rotation of 87 deg was applied to the middle node A of the top end cross section of the tape spring. The prescribed rotations on the edge nodes were then released, and the tape spring was held in this folded configuration for 8 h. To initiate
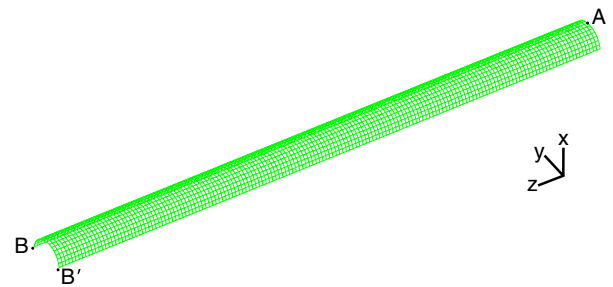

Fig. 13   Finite element model of tape spring.

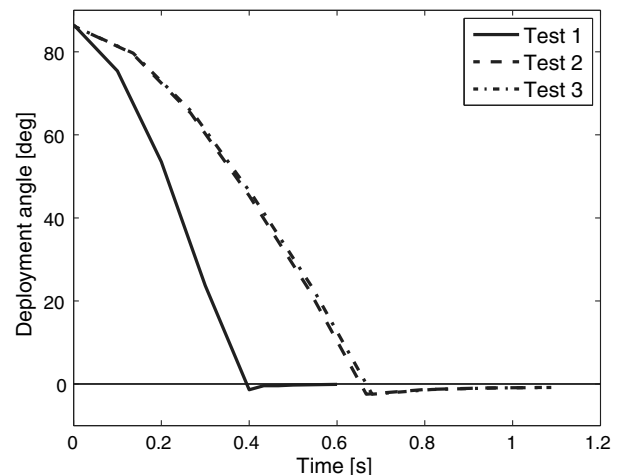**Fig. 12   Experimental configuration.**

Fig. 14   Measurements of deployment angle vs time for tape spring.

deployment, the boundary condition on node A was released instantaneously. The type of analysis was quasi-static for the folding and stowage steps and was switched to dynamic after the removal of the constraint on node A. Gravity loading in the z direction was imposed throughout the simulation. The deployment process was simulated for 8 h. A complete analysis took 40 h to complete on a computer with two Intel Xeon processors running at 2.33 GHz, with four cores per processor.

C. Results

Figure 14 shows plots of the time variation of the deployment angle for the three tests, and Fig. 15 shows a series of intermediate shapes of the tape spring during deployment for test 2. In all tests, the tape spring passed through the vertical (i.e., fully deployed) configuration and overshot by a small amount; afterward, the tape spring gradually straightened, and the deployment angle tended toward zero.
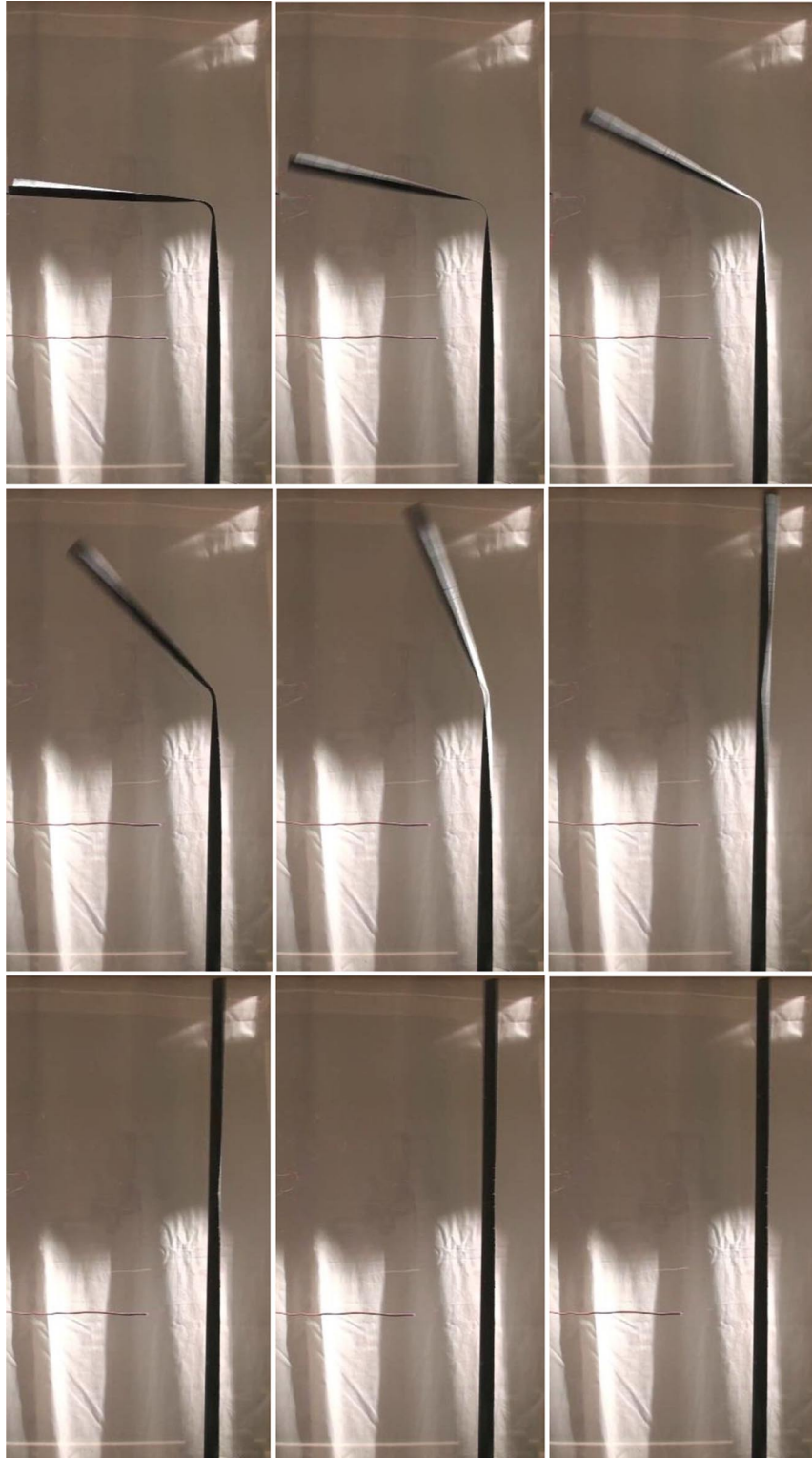

Fig. 15   Snapshots at 0, 0.13, 0.26, 0.39, 0.52, 0.65, 0.78, 0.91, and 1.04 s of deployment sequence in test 2.
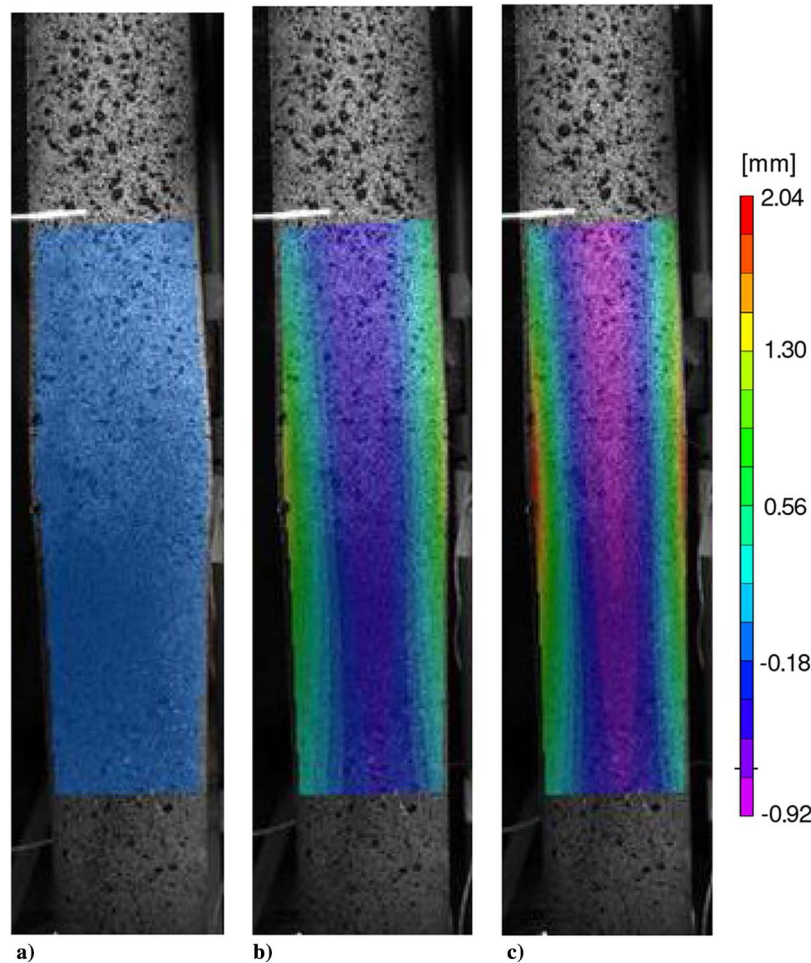
Fig. 16   Measured out-of-plane displacements of fold region relative to the configuration of maximum overshoot: a) at overshoot (reference), b) after 50 s, and c) after 5743 s.

The effect of stowing the tape spring at different temperatures is apparent in Fig. 14. In test 1, the maximum overshoot occurred at 0.4 s and had a magnitude of −1.4°. In test 2, the maximum overshoot was delayed to 0.65 s, and the overshoot angle was −2.5°. The deployment responses for tests 2 and 3 were nearly identical, with only a minor difference in the overshoot time.

These results indicate that the short-term response of the tape spring is affected mainly by the stowage conditions, whereas the deployment temperature has only a minor effect.

Measurements of the out-of-plane displacement field in the fold region of the tape spring during test 2 are shown in Fig. 16. These measurements were obtained by analyzing images of the deformed tape spring with the Vic-3D digital image correlation software. The reference image was taken at the instant of maximum overshoot to capture the details of the cross-section shape change during the final recovery phase. As shown in Fig. 16, the maximum transverse displacement of the tape spring in this region was 3.0 mm (which should be compared to the depth of the tape spring of 16.0 mm), occurring 5743 s (1.6 h) after the configuration of maximum overshoot had been reached. These results indicate that, after deployment, it took a long time for the cross-sectional shape of the tape spring to recover its curvature, although the deployment had nominally been completed in less than 1 s. Hence, it is clear that viscoelastic effects associated with the stowage duration and temperature extend the time needed for full deployment and shape recovery in composite tape springs.

Figure 17 shows a comparison between experimental measurements and finite element simulations of deployment angle vs time, for test 2. Overall, the finite element simulation is in good agreement with the experimentally measured response. In particular, note the close match of the large-rotation behavior, indicating that the
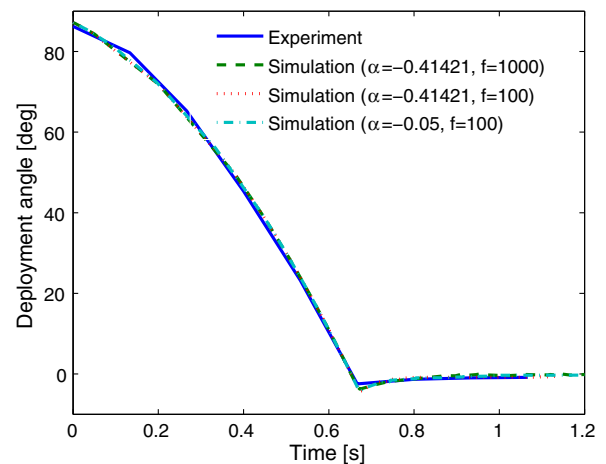

Fig. 17   Comparison of deployment angle vs time for test 2.

model accurately predicts the moment at the fold. Also note in the simulation results that, after ∼0.5 s from the start of deployment, a small vibration develops, due to a torsional oscillation of the upper part of the tape spring. Finally, note that, because of this predicted oscillatory behavior, which was not seen in the experiments, the overshoot angle is overpredicted by about 1.5 deg.

The effects of a much longer stowage period were investigated numerically, using the viscoelastic model. A finite element analysis in which the stowage period was assumed to last one year at 23°C was carried out. The plot of deployment angle vs time obtained from this simulation, shown in Fig. 18, shows a drastically different behavior
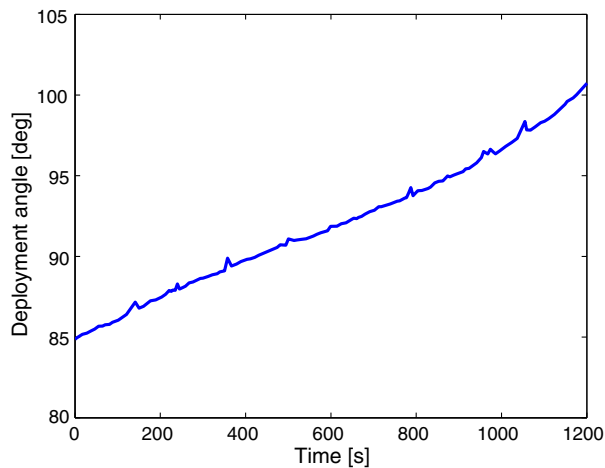
Fig. 18 Predicted incomplete deployment of tape spring that has been held folded for one year.

from that seen previously. According to this prediction, when the tape spring is released, it deploys only a few degrees, and after a slow oscillation, after about 10 days, it reaches a deployment angle of 82.6 deg. This result shows that the fold region of the tape spring has relaxed to such an extent that it is unable to deploy against its own self-weight.

VIII. Conclusions

Fiber-reinforced polymer composites are promising materials for use in lightweight deployable structures. However, the viscoelasticity of this material can significantly affect the deployment of composite space structures after stowage. In this paper, a viscoelastic model for single-ply plain-weave carbon-fabric-reinforced epoxy composites has been developed. The model has been implemented in a structural-scale finite element analysis, and the deployment of tape springs that have been held stowed for different lengths of time and under different temperatures has been studied.

The viscoelastic model is derived from a representative unit cell of the composite material, based on the microstructure geometry, obtained from optical microscopy. The fiber volume density in the tows forming the plain-weave laminas and the constitutive behaviors of the fibers (linear elastic and transversely isotropic) and the matrix (linear viscoelastic) are the key ingredients to set up the model. Finite-element-based homogenizations at two scales, the fiber/matrix and tow scales, have been conducted to obtain the coefficients of the Prony series that characterize their orthotropic behavior, using the measured relaxation modulus of the matrix, which decreases by a factor 3.3 over time span of 1 to 10^{10} s at a temperature of 40°C, as an input. Throughout the model, the relaxation times of the Prony series are set equal to the experimentally derived relaxation times of the matrix Prony series. The outcome of these successive homogenizations is the starting point for the final homogenization step, leading to the lamina relaxation *ABD* matrix, which can be used in studies of the time-dependent behavior of shell structures.

The proposed model has been verified against the experimentally measured time-dependent compliance of a single lamina in pure tension and pure bending, obtaining errors smaller than 5% for tension and 10% for bending.

The stowage and deployment behavior of single-ply tape springs have been studied, both experimentally and through numerical simulations made with the ABAQUS/Standard finite element simulations, where the tape spring was modeled with viscoelastic thin-shell elements. The time-dependent stiffness of the shell elements was modeled through the relaxation *ABD* matrix obtained from the preceding homogenization.

To study the deployment behavior of tape springs after a period of stowage, a ≈90° fold was introduced in a ≈60 cm long tape spring with carbon fibers at ±45° to the axis of the tape spring, and the tape spring was held in this configuration for 8 h and then deployed. This

test was carried out at different temperatures. Images of the deployment behavior showed that the tape spring deploys quickly, overshoots the deployed configuration by a small amount, and then slowly moves toward its final reference configuration. However, the recovery of the cross-section of the tape spring occurs very slowly, over several hours. Extending the duration of the stowage period has the effect of extending the time required for the full deployment. The viscoelastic simulation model captures the experimentally observed deployment behavior with very good accuracy.

A numerical-only study of a single-ply tape spring that is released after being held folded for one year at room temperature has also been presented. It has been shown that, under these conditions, the tape spring is not able to deploy against gravity.

Appendix: Prony Series

Table A1   Relaxation times and Prony coefficients for PMT-F4 epoxy

i	E_i, MPa	ρ_i, s
∞	1000	— —
1	224.1	1.0e + 3
2	450.8	1.0e + 5
3	406.1	1.0e + 6
4	392.7	1.0e + 7
5	810.4	1.0e + 8
6	203.7	1.0e + 9
7	1486.0	1.0e + 10

Table A2   Relaxation times (in seconds) and Prony coefficients (in megapascals) for tows

k	ρ_k	$C_{11,k}$	$C_{12,k}$	$C_{22,k}$	$C_{23,k}$	$C_{55,k}$
∞	— —	150500	2000	6000	2000	2000
1	1.0e + 3	117.1	89.6	242.9	112.0	106.2
2	1.0e + 5	268.7	191.7	512.7	241.4	225.3
3	1.0e + 6	233.6	183.8	518.1	232.3	219.3
4	1.0e + 7	253.8	214.4	538.4	276.1	244.5
5	1.0e + 8	488.2	395.9	1207.9	499.2	480.3
6	1.0e + 9	255.6	359.8	685.9	480.2	366.1
7	1.0e + 10	850.2	644.1	2523.0	761.6	844.4

Table A3   Relaxation times (seconds) and Prony coefficients (newtons per meter) of matrix A

k	ρ_k	$A_{11,k}$	$A_{12,k}$	$A_{33,k}$
∞	— —	740e + 3	110e + 3	155e + 3
1	1.0e + 3	23.3e + 3	4.76e + 3	13.4e + 3
2	1.0e + 5	49.4e + 3	10.3e + 3	27.6e + 3
3	1.0e + 6	49.6e + 3	9.75e + 3	26.4e + 3
4	1.0e + 7	54.0e + 3	12.1e + 3	27.0e + 3
5	1.0e + 8	115.0e + 3	20.5e + 3	56.7e + 3
6	1.0e + 9	80.9e + 3	23.0e + 3	26.5e + 3
7	1.0e + 10	234.0e + 3	29.5e + 3	107.2e + 3

Table A4   Relaxation times (seconds) and Prony coefficients (newton meter) of matrix D

k	ρ_k	$D_{11,k}$	$D_{12,k}$	$D_{33,k}$
∞	— —	919e − 6	30e − 6	160e − 6
1	1.0e + 3	11.7e − 6	10.4e − 6	13.2e − 6
2	1.0e + 5	55.9e − 6	36.5e − 6	40.0e − 6
3	1.0e + 6	8.62e − 6	23.2e − 6	2.03e − 6
4	1.0e + 7	72.0e − 6	29.5e − 6	−8.66e − 6
5	1.0e + 8	45.6e − 6	50.3e − 6	80.8e − 6
6	1.0e + 9	87.5e − 6	52.2e − 6	28.5e − 6
7	1.0e + 10	121.5e − 6	67.4e − 6	84.2e − 6

Acknowledgments

References

[1] Rimrott, F. P. J., "Storable Tubular Extendible Member: A Unique Machine Element," *Machine Design*, Vol. 37, No. 28, Dec. 1965, pp. 156–163.

[2] Seffen, K. A., and Pellegrino, S., "Deployment Dynamics of Tape Springs," *Proceedings of the Royal Society of London, Series A: Mathematical, Physical and Engineering Sciences*, Vol. 455, No. 1983, 1999, pp. 1003–1048.
doi:10.1098/rspa.1999.0347

[3] Seffen, K. A., You, Z., and Pellegrino, Z., "Folding and Deployment of Curved Tape Springs," *International Journal of Mechanical Sciences*, Vol. 42, No. 10, 2000, pp. 2055–2073.
doi:10.1016/S0020-7403(99)00056-9

[4] Watt, A. M., and Pellegrino, S., "Tape-Spring Rolling Hinges," *Proceedings of the 36th Aerospace Mechanisms Symposium*, NASA, May 2002.

[5] Yee, J., and Pellegrino, S., "Composite Tube Hinges," *Journal of Aerospace Engineering*, Vol. 18, No. 4, 2005, pp. 224–231.
doi:10.1061/(ASCE)0893-1321(2005)18:4(224)

[6] Soykasap, O., Pellegrino, S., Howard, P., and Notter, M., "Folding Large Antenna Tape Spring," *Journal of Spacecraft and Rockets*, Vol. 45, No. 3, 2008, pp. 560–567.
doi:10.2514/1.28421

[7] Pellegrino, S., "Folding and Deployment of Thin Shell Structures," *Extremely Deformable Structures*, edited by Bigoni, D., Springer–Verlag, Wien, 2015, pp. 179–267.

[8] Murphey, T. W., Francis, W., Davis, B., and Mejia-Ariza, J. M., "High Strain Composites," *2nd AIAA Spacecraft Structures Conference*, AIAA Paper 2015-0942, 2015.

[9] Seizt, P., "Spar Resolving Spat over Antenna Work," *Space News*, Sept. 1994.

[10] Mobrem, M., and Adams, D., "Deployment Analysis of Lenticular Jointed Antennas Onboard the Mars Express Spacecraft," *Journal of Spacecraft and Rockets*, Vol. 46, No. 2, 2009, pp. 394–402.
doi:10.2514/1.36890

[11] Adams, D., and Mobrem, M., "Lenticular Jointed Antenna Deployment Anomaly and Resolution Onboard the Mars Express Spacecraft," *Journal of Spacecraft and Rockets*, Vol. 46, No. 2, 2009, pp. 403–410.
doi:10.2514/1.36891

[12] Hashin, Z., "Viscoelastic Fiber Reinforced Materials," *AIAA Journal*, Vol. 4, No. 8, 1966, pp. 1411–1417.
doi:10.2514/3.3686

[13] Kwok, K., and Pellegrino, S., "Shape Recovery of Viscoelastic Deployable Structures," *51st AIAA/ASME/ASCE/AHS/ASC Structures, Structural Dynamics, and Materials Conference*, AIAA Paper 2010-2606, April 2010.

[14] Kwok, K., and Pellegrino, S., "Folding, Stowage, and Deployment of Viscoelastic Tape Springs," *AIAA Journal*, Vol. 51, No. 8, 2013, pp. 1908–1918.
doi:10.2514/1.J052269

[15] Domber, J., Hinkle, J., Peterson, L., and Warren, P., "Dimensional Repeatability of an Elastically Folded Composite Hinge for Deployed Spacecraft Optics," *Journal of Spacecraft and Rockets*, Vol. 39, No. 5, 2002, pp. 646–652.
doi:10.2514/2.3877

[16] Soykasap, O., "Deployment Analysis of a Self-Deployable Composite Boom," *Composite Structures*, Vol. 89, No. 3, 2009, pp. 374–381.
doi:10.1016/j.compstruct.2008.08.012

[17] Brinkmeyer, A., Pellegrino, S., and Weaver, P. M., "Effects of Long-Term Stowage on the Deployment of Bistable Tape Springs," *Journal of Applied Mechanics*, Vol. 83, No. 1, Jan. 2016, Paper 011008.
doi:10.1115/1.4031618

[18] Hashin, Z., "Viscoelastic Behavior of Heterogeneous Media," *Journal of Applied Mechanics*, Vol. 32E, No. 3, 1965, pp. 630–636.
doi:10.1115/1.3627270

[19] Hashin, Z., "Viscoelastic Fiber Reinforced Materials," *AIAA Journal*, Vol. 4, No. 8, 1966, pp. 1411–1417.
doi:10.2514/3.3686

[20] Hashin, Z., "Complex Moduli of Viscoelastic Composites—2. Fiber Reinforced Materials," *International Journal of Solids and Structures*, Vol. 6, No. 6, 1970, pp. 797–807.
doi:10.1016/0020-7683(70)90018-1

[21] Li, J., and Weng, G., "Effective Creep Behavior and Complex Moduli of Fiber- and Ribbon-Reinforced Polymer Matrix Composites," *Composites Science and Technology*, Vol. 52, No. 4, 1994, pp. 615–629.
doi:10.1016/0266-3538(94)90044-2

[22] Brinson, L., and Knauss, W., "Finite Element Analysis of Multiphase Viscoelastic Solids," *Journal of Applied Mechanics*, Vol. 59, No. 4, 1992, pp. 730–737.
doi:10.1115/1.2894035

[23] Aboudi, J., "Micromechanical Characterization of the Nonlinear Viscoelastic Behavior of Resin Matrix Composites," *Composites Science and Technology*, Vol. 38, No. 4, 1990, pp. 371–386.
doi:10.1016/0266-3538(90)90022-W

[24] Orozco, C., and Pindera, M., "Viscoelastic Analysis of Multiphase Composites Using the Generalized Methods of Cells," *AIAA Journal*, Vol. 40, No. 8, 2002, pp. 1619–1626.
doi:10.2514/2.1832

[25] Muliana, A., and Haj-Ali, R., "Multiscale Modeling for the Long-Term Behavior of Laminated Composite Structures," *AIAA Journal*, Vol. 43, No. 8, 2005, pp. 1815–1822.
doi:10.2514/1.13830

[26] Govindarajan, S., Langrana, N., and Weng, G., "An Experimental and Theoretical Study of Creep of a Graphite/Epoxy Woven Composite," *Polymer Composites*, Vol. 17, No. 3, 1996, pp. 353–361.
doi:10.1002/(ISSN)1548-0569

[27] Shrotriya, P., and Sottos, N., "Viscoelastic Response of Woven Composite Substrates," *Composite Science and Technology*, Vol. 65, Nos. 3–4, 2005, pp. 621–634.
doi:10.1016/j.compscitech.2004.09.002

[28] Zhu, Q., Shrotriya, P., Geubelle, P., and Sottos, N., "Viscoelastic Response of a Woven Composite Substrate for Multilayer Circuit Board Applications," *Composite Science and Technology*, Vol. 46, 2003, pp. 394–402.

[29] Garnich, M. R., and Hansen, A. C., "A Multicontinuum Approach to Structural Analysis of Linear Viscoelastic Composite Materials," *Journal of Applied Mechanics*, Vol. 64, No. 4, 1997, p. 795.
doi:10.1115/1.2788984

[30] Coleman, B., and Noll, W., "Foundations of Linear Viscoelasticity," *Reviews of Modern Physics*, Vol. 33, No. 2, 1961, pp. 239–249.
doi:10.1103/RevModPhys.33.239

[31] Flugge, W., *Viscoelasticity*, Springer–Verlag, New York, 1975.

[32] Ferry, J., *Viscoelastic Properties of Polymers*, 3rd ed., Wiley, New York, 1980.

[33] Tschoegl, N., *The Phenomenological Theory of Linear Viscoelastic Behavior*, Springer–Verlag, Heidelberg, 1989.

[34] Williams, M., Landel, R., and Ferry, J., "The Temperature Dependence of Relaxation Mechanisms of Amorphous Polymers and Other Glass-Forming Liquids," *Journal of the American Chemical Society*, Vol. 77, No. 14, 1955, pp. 3701–3707.
doi:10.1021/ja01619a008

[35] Park, S. W., and Schapery, R. A., "Methods of Interconversion Between Linear Viscoelastic Materials Functions. Part 1—A Numerical Method Based on Prony Series," *International Journal of Solids and Structures*, Vol. 36, No. 11, 1999, pp. 1653–1675.
doi:10.1016/S0020-7683(98)00055-9

[36] Hilton, H. H., and Yi, S., "The Significance of (An)Isotropic Viscoelastic Poisson Ratio Stress and Time Dependencies," *International Journal of Solids and Structures*, Vol. 35, No. 23, 1998, pp. 3081–3095.
doi:10.1016/S0020-7683(97)00357-0

[37] Technical Data Sheet No. CFA-001, T300 Data Sheet, Toray Industries.

[38] Lee, S., and Knauss, W., "A Note on the Determination of Relaxation and Creep Data from Ramp Tests," *Mechanics of Time-Dependent Materials*, Vol. 4, No. 1, 2000, pp. 1–7.
doi:10.1023/A:1009827622426

[39] Daniel, M., and Ishai, O., *Engineering Mechanics of Composite Materials*, Oxford Univ. Press, Oxford, 2006.

[40] *ABAQUS/Standard, Ver. 6.7*, Simulia, Providence, RI, 2007.

[41] Kueh, A., and Pellegrino, S., "*ABD* Matrix of Single-Ply Triaxial Weave Fabric Composites," *48th AIAA/ASME/ASCE/AHS/ASC Structures, Structural Dynamics and Materials Conference*, AIAA Paper 2007-2161, April 2007.

R. Ohayon
Associate Editor